

Physics-dynamics coupling with element-based high-order Galerkin methods: quasi equal-area physics grid

ADAM R. HERRINGTON*

School of Marine and Atmospheric Sciences, Stony Brook University, Stony Brook, New York, USA.

PETER H. LAURITZEN

Climate and Global Dynamics, National Center for Atmospheric Research, 1850 Table Mesa Drive, Boulder, Colorado, USA.

MARK A. TAYLOR

Sandia National Laboratories, Albuquerque, New Mexico, USA.

STEVE GOLDHABER

Climate and Global Dynamics, National Center for Atmospheric Research, 1850 Table Mesa Drive, Boulder, Colorado, USA.

KEVIN A. REED

School of Marine and Atmospheric Sciences, Stony Brook University, State University of New York, Stony Brook, New York.

PAUL A. ULLRICH

Department of Land, Air and Water Resources, University of California, Davis, California, USA.

ABSTRACT

Atmospheric modeling with element-based high-order Galerkin methods presents a unique challenge to the conventional physics-dynamics coupling paradigm, due to the highly irregular distribution of nodes within an element, and the distinct numerical characteristics of the Galerkin method. The conventional coupling procedure is to evaluate the physical parameterizations ('physics') on the dynamical core grid. Evaluating the physics at the nodal points exacerbates numerical noise from the Galerkin method, enabling and amplifying local extrema at element boundaries. Grid imprinting may be substantially reduced through the introduction of an entirely separate, approximately isotropic finite-volume grid for evaluating the physics forcing. Integration of the spectral basis over the control-volumes provides an area average state to the physics, which is more representative of the state in the vicinity of the nodal points rather than the nodal point itself, and is more consistent with the notion of a 'large-scale state' required by most physics packages. This study documents the implementation of a quasi-equal area physics grid into NCAR's Community Atmosphere Model with Spectral Elements, and is shown to be effective at mitigating grid imprinting in the solution. The physics grid is also appropriate for coupling to other components of the Community Earth System Model, since the coupler requires component fluxes to be defined on a finite-volume grid, and one can be certain that the fluxes on the physics grid are indeed, volume-averaged.

1. Introduction

An increasing number of numerical methods publications in the atmospheric science literature concern trans-

port, shallow-water, and three-dimensional models employing element-based high-order Galerkin discretizations such as finite-element and discontinuous Galerkin methods (for an introduction to these methods see, e.g., Durran 2010; Nair et al. 2011). Some global models based on Galerkin methods have reached a level of maturity for which they are being considered for next generation climate and weather models due to their inherent conser-

*Corresponding author address: Adam R. Herrington, School of Marine and Atmospheric Sciences, Stony Brook University, Stony Brook, New York, USA.

E-mail: adam.herrington@stonybrook.edu



FIG. 1. Example of CAM-SE GLL quadrature grids, marked with red filled circles, (a & c) on the cubed-sphere and (b & d) in an element. (a)-(b) and (c)-(d) use 4×4 ($np = 4$) and 8×8 ($np = 8$) GLL quadrature points in each element, respectively. (a) and (c) have the same average grid-spacing at the Equator (7.5°) which is obtained by using (a) 4×4 ($ne = 4$) and (b) 2×2 ($ne = 2$) elements on each cubed-sphere face/panel, respectively. The element boundaries are marked with thick light blue lines. The grid configurations shown on (a) and (c) are referred to as $ne4np4$ and $ne2np8$, respectively.

vation properties, high-order accuracy (for smooth problems), high parallel efficiency, high processor efficiency, and geometric flexibility facilitating mesh-refinement applications. NCAR's Community Atmosphere Model (CAM; Neale et al. 2012) offers a dynamical core based on continuous Galerkin finite elements (Taylor and Fournier 2010), referred to as CAM-SE (CAM Spectral Elements; Dennis et al. 2012; Taylor et al. 2008; Lauritzen et al. 2018). CAM-SE is, in particular, being used for high resolution climate modeling (e.g., Small et al. 2014; Reed et al. 2015; Bacmeister and Coauthors 2018) and static mesh-refinement applications (e.g., Fournier et al. 2004; Zarzycki et al. 2014a,b; Guba et al. 2014b; Rhoades et al. 2016). Other examples of models based on high-order Galerkin methods that are being considered for ‘operational’ weather-climate applications are Giraldo and Restelli (2008), Nair et al. (2009) and Brdar et al. (2013).

Assumptions inherent to the physical parameterizations (also referred to as *physics*) require the state passed by the dynamical core to represent a ‘large-scale state’, for example, in quasi-equilibrium-type convection schemes (Arakawa and Schubert 1974; Plant 2008). In finite-volume methods, one may think of the dynamical core state as the average state of the atmosphere over a control volume,

and for resolutions typical of climate simulations is entirely consistent with the notion of a ‘large-scale state’. For finite-difference methods the point value is thought of as representative for the atmospheric state in the vicinity of the point value and one can usually associate a volume with the grid-point. Hence the physics grid (the grid on which the state of the atmosphere is evaluated and passed to physics) and the dynamics grid (the grid the dynamical core uses) coincide. Having the physics and dynamics grids coincide is obviously convenient since no interpolation is needed (which could disrupt conservation properties) and the number of degrees of freedom on both grids is exactly the same.

For the regular latitude-longitude, cubed-sphere and icosahedral grids the distance between the grid-points is gradually varying for finite-volume/finite-difference discretizations. For high-order element-based Galerkin methods, the dynamical core grid is defined by the quadrature points. For the case of CAM-SE these are the Gauss-Lobatto-Legendre (GLL) quadrature nodes. A unique aspect of the high-order quadrature rules is that the nodes within an element are not equally spaced. For example, Figure 1 shows GLL points on an individual element of a cubed-sphere grid for degree 3 ($np = 4$ quadrature points) and degree 7 ($np = 8$ quadrature points) polynomial basis in CAM-SE. Both grids have the same average resolution on the sphere (due to different number of elements), however, the higher the order of the quadrature rule the less equi-distant are the quadrature points. GLL quadrature points cluster near the edges and, in particular, the corners of the elements.

If the conventional physics-dynamics coupling paradigm is applied to CAM-SE, then the physics are evaluated at the GLL nodes, and a volume associated with the quadrature point should be defined. An example of that is shown on Figure 2 where control volumes have been defined around the quadrature points so that the spherical area of the control volumes exactly match the Gaussian weight multiplied by the metric term (these weights are used for integrating the basis functions over the elements and can therefore, in this context, be interpreted as areas). [Mark: could we be mathematically more rigorous? perhaps an appendix describing the iterative algorithm?] This grid is used in the NCAR CESM (Community Earth System Model) coupler for passing states between ocean, atmosphere and land components since the current remapping method is finite-volume based and therefore requires control volumes¹. Hence the components ‘see’ an irregular atmospheric grid. Similarly, the parameterizations in the atmosphere ‘see’ a state that is anisotropically sampled in space (see Figure 1 and 5 in Kim et al. 2008).

It would be incorrect to interpret the irregular size of control volumes in Figure 2 as an equivalent spread in

¹it is noted that methods exist that do not require control volumes for conservative interpolation (Ullrich and Taylor 2015)

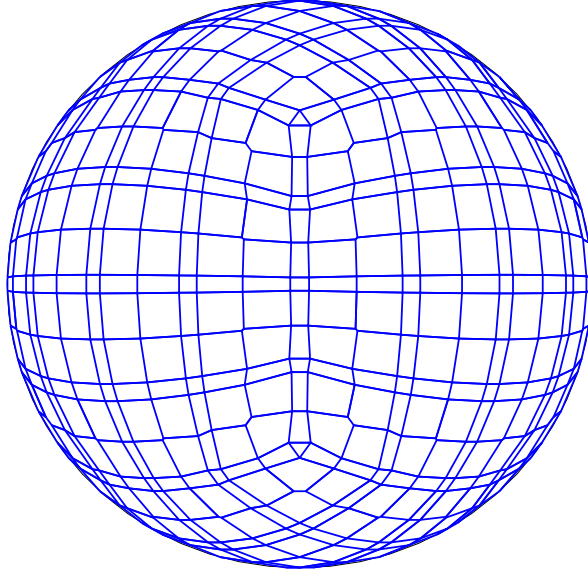


FIG. 2. An example of control volumes constructed around GLL quadrature points (NE4NP4) so that the spherical area of the control volumes exactly match the quadrature weight multiplied by the metric factor.

the scales of motion resolved by the dynamical core. The scales of motion are defined by the degree of the Lagrange basis in each element, and the nodes may be viewed as irregularly spaced samples of an underlying spectrally truncated state. From this perspective, one might expect the solution to be independent of control volume size. An aqua-planet simulation (Neale and Hoskins 2000; Medeiros et al. 2016) is carried out using CAM-SE (Figure 3), and the probability density distribution of the upward vertical pressure velocity (ω), conditionally sampled based on three categories - ‘interior nodes’, with their large grid cell areas, and ‘edge’ and ‘corner’ nodes with their characteristically smaller grid cell areas - is shown in Figure 3. There is an apparent dependence on control volume size, with interior nodes being characteristically sluggish and initially at odds with the expectation. However, the lack of a distinction between ‘corner’ and ‘edge’ solutions is consistent with our expectation. It turns out, that ‘corner’ and ‘edge’ solutions are similar because they have something else in common - they both lie on an element boundary. The division of solutions shown in Figure 3 is primarily between whether a node is, or is not situated on an element boundary, and is a nuanced signature of high-order element-based Galerkin methods for non-smooth problems.

The quadrature grid in element-based Galerkin methods is defined to perform mathematical operations on the basis functions, e.g., computing gradients and integrals, rather

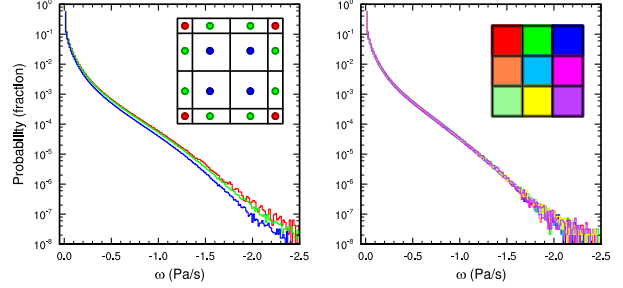


FIG. 3. Probability density distribution of instantaneous upward ω in a pair of aqua-planet simulations using CAM4 physics. Figure is constructed from one year of six hourly data, at all vertical levels. (Left) *ne30np4* configuration conditionally sampled for interior, edge and corner node control volumes, and (Right) *ne30pg3* configuration, but sampled by within-element physics grid-cell location. Note the consistently larger magnitude ω for boundary nodes compared with interior nodes, and that the bias is eliminated through mapping to a quasi-equal area physics grid.

than evaluating the state variables for physics-dynamics coupling. While the interior quadrature nodes are high-order C^∞ in CAM-SE, the smoothness of boundary nodes are constrained by the need to patch neighboring solutions together to form a globally continuous solution, known as the direct stiffness summation (DSS). The DSS operation is attractive because it allows for high-order accuracy with minimal communication between elements, but results in a C^0 degradation at element boundaries (Figure 4). Through evaluating the physics at the nodal points, strong grid-scale forcing or oscillatory behavior near an element boundary may exacerbate the discontinuity (Figure 4). The greater magnitude vertical motion of boundary nodes in Figure 3 is therefore due to the systematically tighter pressure gradients on element boundaries. One may argue that it would be more consistent to integrate the basis functions over quasi-equal area control volumes within each element and pass those control volume average values to physics rather than irregularly spaced quadrature point values. In this case when integrating basis functions over control volumes a grid-cell average value is more representative of the values near the extrema at the element boundary than the quadrature point value. The relationship between the nodal values, the basis functions and the proposed control volumes is illustrated schematically in one-dimension in Figure 5.

It is the purpose of this paper to document the implementation of a quasi-equal area physics grid into CAM-SE, in which the physics and dynamics grids are entirely separated as illustrated in one dimension in Figure 5, and the impact on model solution. The implementation of the physics grid configuration into CAM-SE is presented in Section 2. Idealized model configurations with and without topography are presented in Section 3, illustrating the

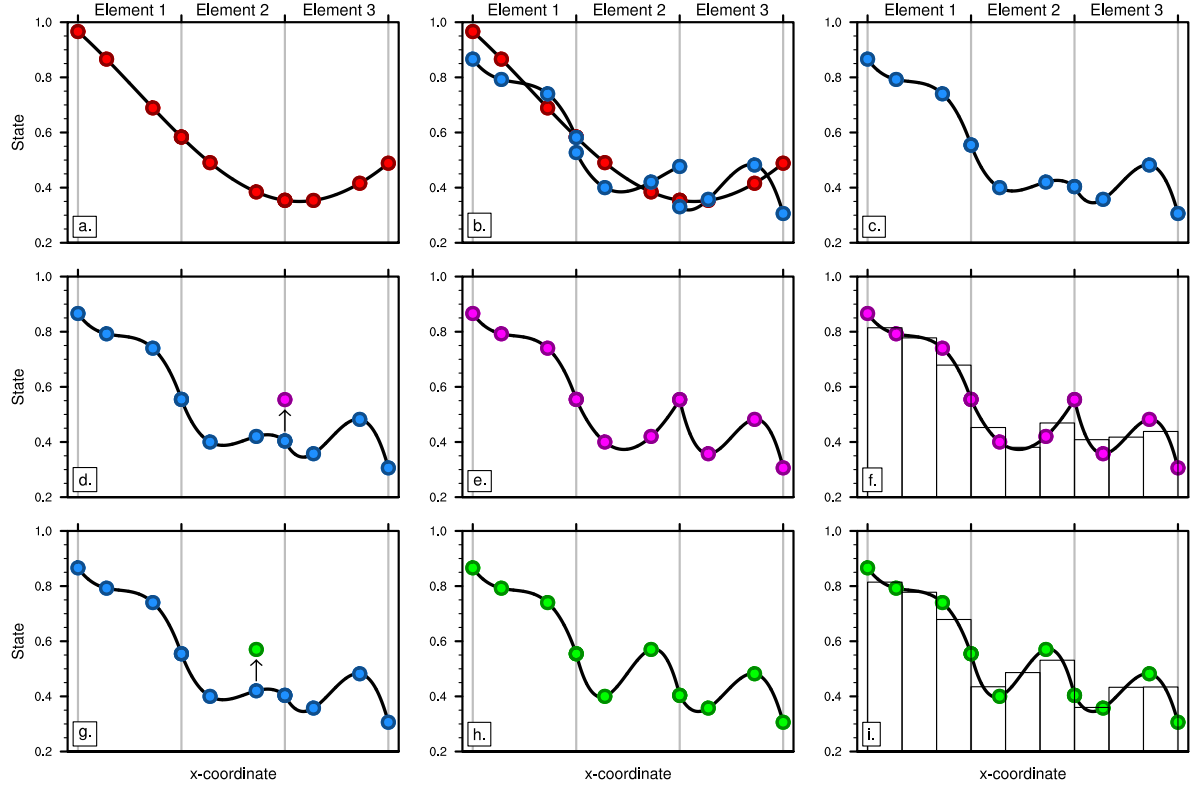


FIG. 4. A one-dimensional schematic illustration on how CAM-SE advances the solution to the equations of motion in time. Consider a transect across three elements. The filled circles are the GLL quadrature points in each element ($np = 4$). Note that the quadrature points on the boundary are shared between elements. (a) Smooth initial condition. (b) The solution to the equations of motion are advanced in time (one Runge-Kutta step) independently in each element leading to the quadrature values marked with filled blue circles. The Lagrange basis is shown as curves connecting the blue circles. There are now two solutions, one from left and one from right, for the quadrature points at the element boundaries. In CAM-SE a numerical flux is applied to the element boundary that results in a simple average of the two nodal values, but degrades the boundary nodes to C^0 . Note that the averaging changes the Lagrange polynomials throughout except at the internal quadrature points. (c) shows the solution after applying the boundary flux. (d) Assume there is a grid-scale physics forcing that increases the quadrature value at the location of the arrow. (e) The solution is now clearly C^0 at the element boundary. (f) Vertical bars indicate the average values resulting from integrating the basis functions over the control volumes of the quasi-equal area physics grid. (g)-(i), repeats the scenario of (d)-(f), but instead with a forcing applied to an interior node (arrow in (g)), illustrating the C^∞ smoothness of interior nodes.

physics grid is effective at mitigating undesirable grid imprinting in the solution. Section 4 contains a discussion of results and concluding remarks.

2. Methods

Here we focus on CAM-SE, however, in principle the methods apply to any element-based high-order Galerkin model. The physics grid in CAM-SE is defined by subdividing each element using equi-angular gnomonic coordinate lines to define the sides of the physics grid control volumes. Note that the element boundaries are defined by equi-angular gnomonic grid lines. The notation $pg = 3$ refers to the configuration where the elements are divided into $pg \times pg = 3 \times 3$ quasi equal-area physics grid cells (see Figure 6). Defining the physics grid by sub-diving

elements makes it possible to use the same infrastructure as used for the quadrature point values thereby facilitating its implementation in CAM-SE. Here we make use of the $ne30np4$ and $ne30pg3$ grids that use GLL quadrature point physics grid (physics and dynamics grid coincide), and the same ($pg = 3$) resolution quasi equal-area physics grids, respectively. In all configurations we use degree three Lagrange basis ($np = 4$) and $ne \times ne = 30 \times 30$ elements on each cubed-sphere panel resulting in an average GLL quadrature point spacing at the Equator of 1° .

Separation of the physics and dynamics grids was made possible through the implementation of the Conservative Semi-Lagrangian Multi-tracer transport scheme in CAM-SE (CAM-SE-CSLAM; Lauritzen et al. (2017)). Tracers evolve in CSLAM using a semi-lagrangian method on the

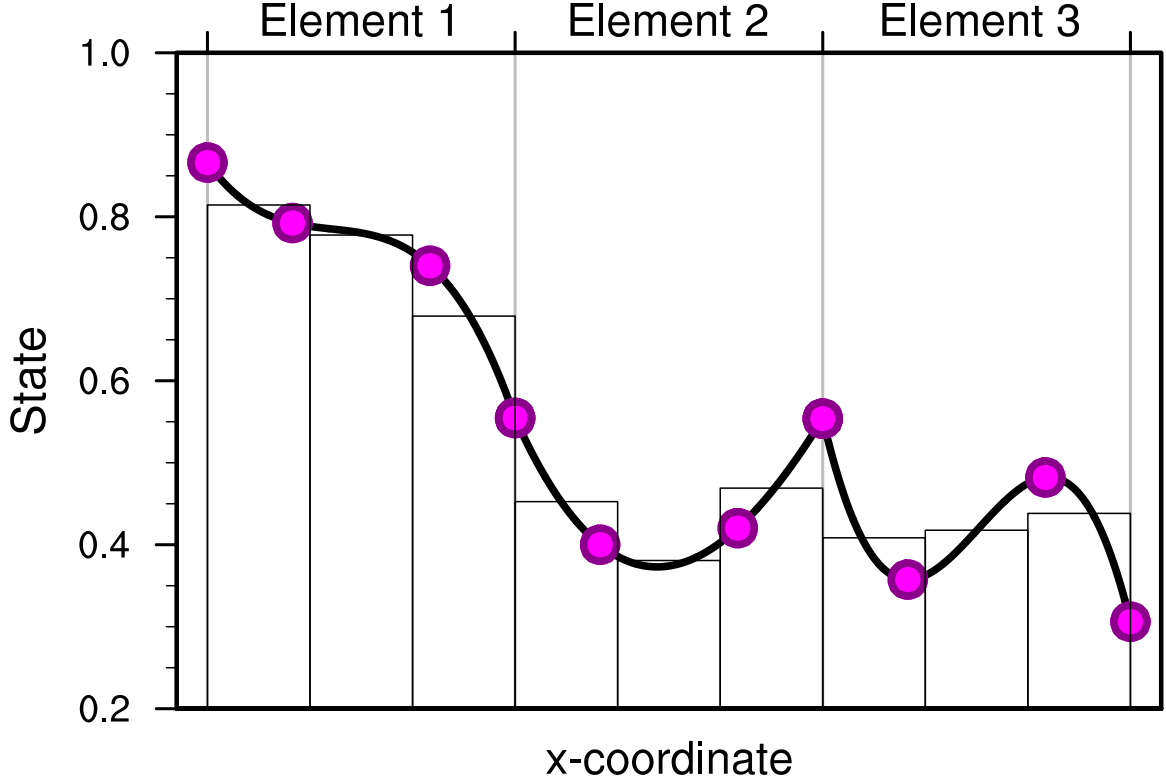


FIG. 5. A graphical illustration of the physics grid in one dimension. Three elements are shown and the filled red circles are the GLL quadrature points in each element. The red curve is the basis function representation of the field and the green filled circles are the quadrature point values. The physics grid divides each element into 3 equal-area control volumes. The histogram shows the average values over the physics grid control volumes resulting from integrating the basis functions over the respective control volumes.

$pg = 3$ finite-volume grid (Figure 5). The physics grid configuration is distinct from CAM-SE in that it uses the finite-volume grid to compute the physics and the tracers, using CSLAM. For this reason, the physics grid configuration is referred to as CAM-SE-CSLAM throughout the study.

A consequence of separating physics and dynamics grids is that the atmospheric state must be mapped to the physics grid and the physics tendencies must be mapped back to the dynamics grid. This is discussed in separate sections below.

a. Mapping state from dynamics grid (GLL) to physics grid (physgrid)

The dynamics state is defined on the GLL grid in terms of temperature $T^{(gll)}$, zonal wind component $u^{(gll)}$, meridional wind component $v^{(gll)}$, and dry pressure level thickness $\Delta p^{(gll)}$. In the mapping of the atmospheric state to the physics grid it is important that the following properties are met:

1. conservation of scalar quantities such as mass and dry thermal energy,
2. for tracers; shape-preservation (monotonicity), i.e. the mapping method must not introduce new extrema in the interpolated field, in particular, negatives,
3. consistency, i.e. the mapping preserves a constant,
4. linear correlation preservation.

Other properties that may be important, but not pursued here, is total energy conservation and axial angular momentum conservation. We argue that the most consistent method for mapping scalar state variables from the GLL grid to the physics grid is to integrate the Lagrange basis functions representation (used by the SE dynamical core) over the physics grid control volumes, i.e. integrate the basis function representation of $\Delta p^{(gll)} \times T^{(gll)}$ and $\Delta p^{(gll)}$ over the physics grid control volume (see, e.g., Lauritzen

$$np = 4 \quad pg = 3$$

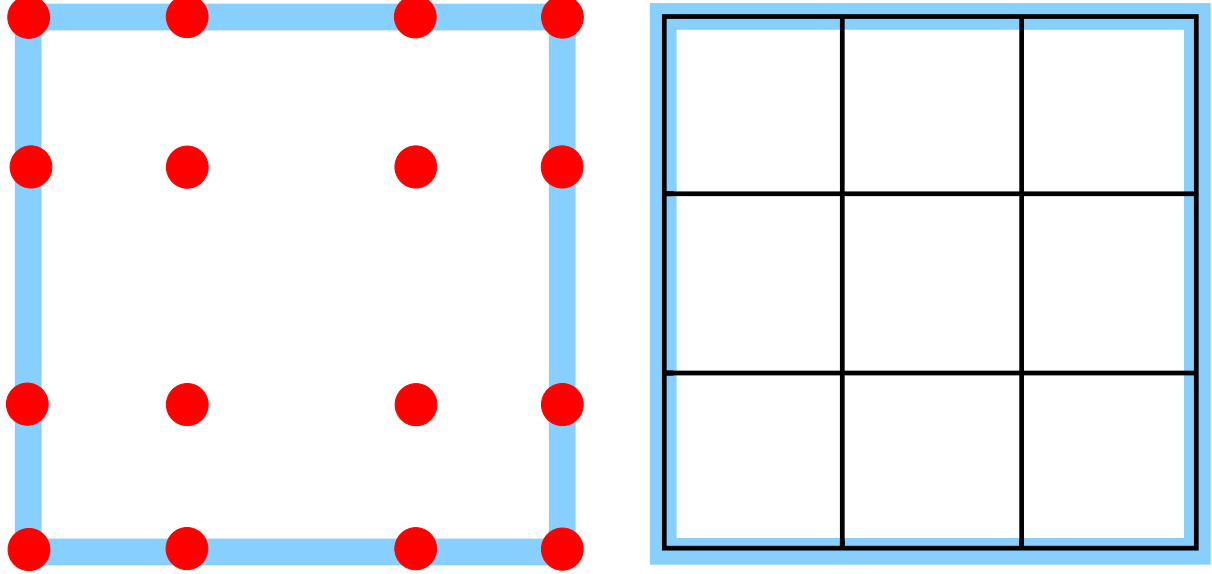


FIG. 6. A schematic illustration of an element, indicating the relationship between (left) the dynamical core grid, and (right) the proposed quasi-equal area physics grid. The physics grid contains $pg \times pg = 3 \times 3$ grid cells in each element.

et al. 2017; Ullrich and Taylor 2015)

$$\begin{aligned} \Delta p^{(physgrid)} &= \frac{1}{A^{(physgrid)}} \int_{A^{(physgrid)}} \Delta p^{(gll)} dA, \\ T^{(physgrid)} &= \frac{1}{A^{(physgrid)} \Delta p^{(physgrid)}} \int_{A^{(physgrid)}} T^{(gll)} \Delta p^{(gll)} dA \end{aligned}$$

where $A^{(physgrid)}$ is the physics grid area. The integrals are numerically computed using the GLL quadrature rule. Thermal energy and dry air mass is conserved and the mapping is consistent. For the wind, which is a vector, the latitude-longitude wind components are mapped by transforming to contra-variant wind components, evaluate the basis function representation thereof at the equi-angular center of the physics grid control volumes and then transform back to latitude-longitude coordinate system winds. All of the operations are local to the element and do not require communication between elements.

The mapping of tracers is more problematic since the SE basis function representation is oscillatory although the shape-preserving filter guarantees shape-preservation at the GLL nodes (Guba et al. 2014a). To avoid this issue we use the CAM-SE-CSLAM version of CAM-SE where tracers are advected on the 3x3 physics grid. Note that in CAM-SE-CSLAM the dry mass internally predicted by CSLAM, $\Delta p^{(cslam)}$, is, by design, equal to $\Delta p^{(gll)}$ integrated over the CSLAM/physics grid control volume (Lauritzen et al. 2017). Since the tracer grid and physics

grids are co-located and $\Delta p^{(physgrid)} = \Delta p^{(cslam)}$ then the mass conservation, correlation preservation, consistency and shape-preservation constraints are inherently fulfilled.

Mapping tendencies from physics grid (physgrid) to dynamics grid (GLL)

The physics tendencies are computed on the finite-volume physics grid and are denoted $f_T^{(phys)}$, $f_u^{(phys)}$, $f_v^{(phys)}$, and $f_m^{(phys)}$. Note that dry air mass is not modified by physics and hence there is no tendency for dry mass, $f_{\Delta p} \equiv 0$. Also, it is important to map tendencies and not state from the physics grid to GLL grid otherwise one will get spurious tendencies from mapping errors when the actual physics tendency is zero (unless a reversible map is used).

It is important that this process:

1. preserves a zero tendency,
2. for tracers; mass tendency is conserved,
3. for tracers; in each tracer grid cell the mass tendency from physics must not exceed tracer mass available in tracer grid cell (it is assumed that the physics tendency will not drive tracer mixing ratio negative on the physics grid),
4. linear correlation preservation,

5. consistency, i.e. the mapping preserves a constant.

Other properties that may be important, but not pursued here, is total energy conservation (incl. components of total energy) and axial angular momentum conservation. Scalar variables are mapped from physics grid to GLL grid using a tensor-product Lagrange interpolation. The local coordinates on a cubed-sphere are discontinuous at the element edges so the interpolation requires special attention at the cube corners and edges. The details are provided in Appendix 4. Lagrange interpolation preserves a constant (including zero) and linear correlations. Tracer and physics grids are co-located so tracer mass, tracer shape, and tracer correlations are trivially preserved on the tracer grid; and the inconsistency in point 3 above will not appear.

We do, however, need to map water tracers (such as water vapor, cloud liquid and cloud ice) to the GLL grid to account for moist effects in the equations of motion solved on the GLL grid. The CSLAM water tracer mixing ratios updated by physics tendencies are mapped to the GLL grid using the same tensor cubic interpolation as is used for temperature and velocity components. In between the calls to physics (i.e. in the dynamical core sub-stepping) the water tracers are advected on the GLL grid with the SE method. Water tracer mass is not conserved in the mapping from tracer/physics grid to GLL grid. This procedure makes sure that the water tracers on the GLL grid are 'nudged' to the CSLAM solution for water tracers and the mass budget is closed on the tracer/physics grid.

In the mapping algorithm from physics to dynamics it was found (a) important to use an algorithm that is smooth across element boundaries and (b) that obtaining mass-conservation without excessive grid imprinting at element edges difficult. In regard to (a), using an algorithm that only uses information from an element of control volumes will (at best) be C^0 at the element boundaries where most of the GLL points are located. A stencil that extends beyond one element is necessary. Mass-conservation requires a control volume to be defined around the GLL points (see, e.g., Figure 2 in this paper or Figure 8b in Ullrich et al. 2016). These volumes are artificial and not consistent with the SE method. Integrating the CSLAM reconstruction of water tracers of such artificial control volumes led to GLL node grid imprinting in the mapping and will not preserve a constant mixing ratio since the mapping of $\Delta p^{(physgrid)}$ to GLL will not yield the GLL node value for dry pressure-level thickness (i.e. the maps are not reversible). Hence, after much experimentation, best results in terms of grid-imprinting and conservation were obtained with tensor-cubic interpolation and by using the CAM-SE-CSLAM configuration.

- in results section we might want to show some energy diagnostics and estimate PDC errors; must be run with cp_{dry}

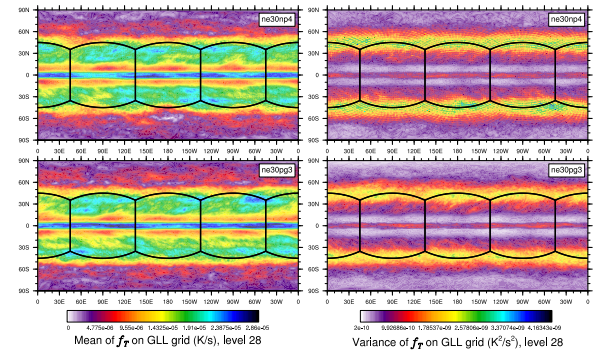


FIG. 7. Mean (left) and variance (right) of the low level temperature tendencies from the physical parameterizations on the GLL grid, with the *ne30np4* configuration, top row) and *ne30pg3* configuration (bottom row), in a pair of year-long aqua-planet simulations after Medeiros et al. (2016). Grid imprinting is observed along the element boundaries in *ne30np4*, but is absent from the *ne30pg3* simulation.

3. Results

The CAM aqua-planet reference configuration (Neale and Hoskins 2000; Medeiros et al. 2016) consists of an ocean covered planet in a perpetual equinox, with fixed, zonally symmetric SST temperatures idealized after the present day climatology. Two year long aqua-planet simulations are performed using CAM-SE in the *ne30np4* configuration, and CAM-SE-CSLAM in a *ne30pg3* configuration. A plot similar to Figure 3 is constructed for the *ne30pg3* simulation, in which a probability density distribution of upward ω in the deep tropics is conditionally sampled based on location within the element. In the *ne30pg3* configuration, the sampling is based on a grid cell index 1-9, corresponding to the control volume location within the element (Figure 3). Through the use of the physics grid, the dynamical state appears independent of location within the element, a marked improvement over the *ne30np4* configuration (Figure 3). Since the state is independent of in-element location, it follows that the physics forcing, which is evaluated from the state, should also be independent of within-element location. The low-level, mean and variance of the physics tendencies in the two aqua-planet simulations are shown in Figure 7. The mean physics tendencies contains modest grid imprinting in the default configuration, while in the variance field, grid imprinting is both ubiquitous and unmistakable (Figure 7). The variance is larger on boundary nodes (Figure 7), manifesting as a 'stitching' pattern resembling the cube-sphere grid. In *ne30pg3*, the grid imprinting is all but eliminated based on the mean and variance of the physics tendencies (Figure 7).

Grid imprinting associated with the flow around obstacles is more problematic than that encountered on the

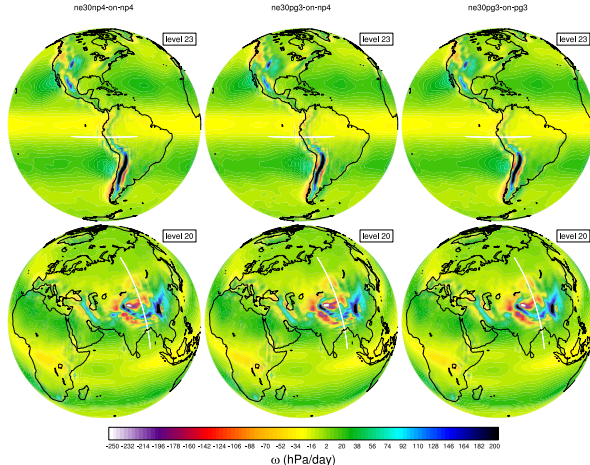


FIG. 8. Mean ω at two model levels in the middle troposphere, in a Held-Suarez configuration outfitted with real world topography. (Left) CAM-SE state on the GLL grid, *ne30np4*, (Middle) CAM-SE-CSLAM state on the GLL grid, *ne30np4* and (Right) CAM-SE-CSLAM state on the physics grid, *ne30pg3*. The ω fields are computed from a 1200 day Held-Suarez simulation. White lines denote the great circle transects in 9.

aqua-planets. In order to diagnose grid imprinting associated with topographic flow, an idealized held-suarez configuration (Held and Suarez 1994) is outfitted with real world topography, and ran for a year using the *ne30np4* and *ne30pg3* configurations. Figure 8 shows the mean ω at two different vertical levels in the middle troposphere. At higher latitudes (such as southern Andes), the flow is smooth, conforming reasonably to the underlying topography. At lower latitudes, over the Andes or the Himalayas, there is a clear preference for larger magnitude vertical motion to occur at the element boundaries. The vertical structure of ω in regions of strong grid-imprinting is depicted in Figure 9, which are great-circle distance-pressure transects over the Andes and Himalayas. The ω field indicates large magnitude upward motion occurs as the flow approaches the foot of a topographic obstacle. Compensating downward motion tends to occur a couple of nodes downwind of the strong upward motion (although sometimes they form up-wind). The full troposphere upward-downward couples are an indication that grid imprinting due to topography is enhanced in regions of weak stratification, such as occurs in the deep tropics, with forced upslope flow facilitating the release of gravitational instability. The greater magnitude vertical motion is a result of the characteristically tighter pressure gradients at element boundaries.

Through the use of the quasi-equal area physics grid, grid imprinting due to topographic flow is reduced (Figures 8 and 9). Figures 8 and 9 also show the state in CAM-SE-CSLAM, but on the dynamical core grid. Arguably,

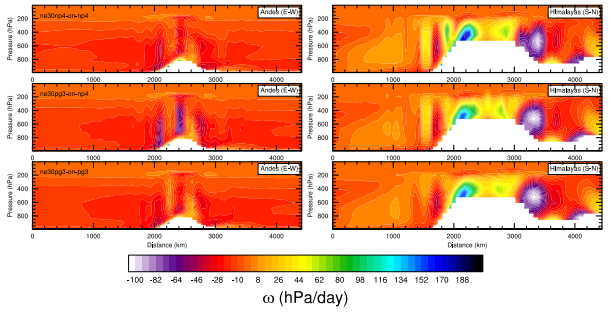


FIG. 9. Great circle distance-pressure transect of ω in the Held-Suarez simulations with realistic topography. The ω field is computed from a 1200 day simulation.

grid imprinting due to topography in CAM-SE-CSLAM is not much of an improvement over CAM-SE, from the perspective of the dynamical core grid. Some regions (e.g., the Andes) appear to have a larger grid imprinting signal, relative to CAM-SE, while other regions (e.g., Himalayas) indicate an improvement. The native topography lives on the physics grid, and the surface geopotential is mapped to the nodal points at run-time in CAM-SE-CSLAM. Mapping topography to the quadrature nodes ensures that no new extrema will be introduced to the boundary nodes, where the solution is least smooth. This effect can not be very large, apparent from the conflicting influence of the physics grid on grid imprinting on the dynamical core grid. From the perspective of the physics grid, the CAM-SE-CSLAM solution clearly contains less grid imprinting compared to CAM-SE (Figures 8 and 9). The reduction in grid imprinting in CAM-SE-CSLAM is therefore almost entirely a result of the smoothing effect of integrating the basis functions over the control volumes of the physics grid.

4. Conclusions

Element-based high-order Galerkin Methods possess many of the attractive qualities recommended for next generation global atmospheric models. Among these, high-order accuracy is achieved with minimal communication between elements, allowing for near perfect scaling on massively parallel systems. Element communication amounts to a numerical flux applied to the element boundaries, reconciling overlapping solutions of adjacent elements but degrading the order of accuracy of the boundary nodes in the process (to C^0) **Peter - is order of accuracy not the same thing?** For non-smooth problems, gradients are systematically tighter at the element boundaries, and local extrema often characterize the boundary nodes. This behavior is illustrated using NCAR's Community Atmosphere Model with Spectral Elements dynamics (CAM-

SE) in an aqua-planet configuration, and in a Held-Suarez configuration with real-world topography.

The authors argue that the conventional physics-dynamics coupling paradigm, in which the physical parameterizations are evaluated on the dynamical core grid, exacerbates grid imprinting by commuting boundary node extrema through the physics forcing. A separate physics grid is proposed and implemented in CAM-SE, and referred to as CAM-SE-CSLAM, through dividing the elements into quasi-equal areas with equivalent degrees of freedom. The state is mapped to the physics grid with high-order accuracy through integrating CAM-SE's Lagrange basis functions over the control volumes. Control volumes near element boundaries now represent a state in the vicinity of the extrema produced through the boundary exchange operation, as opposed to the the nodal value itself. The physical parameterizations are evaluated on the finite volume grid, and the forcing terms are mapped back to the dynamical core grid [discuss mapping back](#). In aqua-planet simulations, evaluating the parameterizations on the physics grid removes any obvious dependence of proximity to the element boundary, resulting in a more realistic state with negligible grid imprinting.

In CAM-SE-CSLAM, the physics grid replaces the default finite-volume grid used to compute fluxes between model components in CAM-SE (Figure ??). The appeal here is two-fold. Through integrating the Lagrange basis functions over control volumes, one can be certain that the fluxes computed from this grid are indeed a volume averaged flux. The same can not be said for CAM-SE, where the nodal values are effectively assigned to each control volume. The second advantage of the new coupler grid, is that extrema occurring on boundary nodes can no longer commute through other model components, in simulations without topography. Topographically induced grid imprinting is reduced through the use the physics grid, primarily through the smoothing effect of integrating the basis functions over the control volumes on the physics grid, although grid imprinting is still observed in the mean state. The quasi-equal area physics grid is nonetheless, effective at mitigating numerical nuances associated with high-order element-based Galerkin methods, for non-smooth problems.

Acknowledgments. NCAR is sponsored by the National Science Foundation (NSF).

APPENDIX

The mapping of the physics tendencies from the physics grid to the GLL grid is done with tensor-cubic Lagrange interpolation.

The coordinate used for the interpolation is a non-dimensional reference coordinate $(\xi^1, \xi^2) \in [-1 : 1]^2$ also used internally in the SE dynamical (see, e.g., section

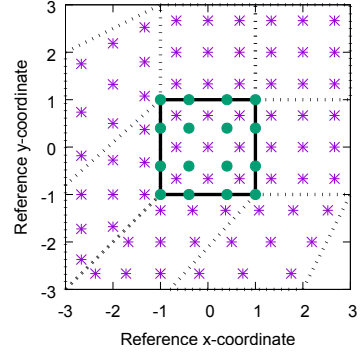


FIG. A1.

3.3 in Lauritzen et al. 2018). The elements of the cubed-sphere in SE are created from an equi-angular gnomonic projection. Consider one element $(\alpha, \beta) \in (\alpha_1^{(elem)}, \alpha_2^{(elem)}) \times (\beta_1^{(elem)}, \beta_2^{(elem)})$ where (α, β) are central angle coordinates. Let $\Delta\alpha^{(elem)} = \alpha_2^{(elem)} - \alpha_1^{(elem)}$ and $\Delta\beta^{(elem)} = \beta_2^{(elem)} - \beta_1^{(elem)}$. The physics grid cell central angle centers are located at

$$(\alpha_i^{(phys)}, \beta_j^{(phys)}) = \left[\alpha_1^{(elem)} + (i - \frac{1}{2}) \Delta\alpha^{(phys)}, \beta_1^{(elem)} + (j - \frac{1}{2}) \Delta\beta^{(phys)} \right] \quad (A1)$$

where $\Delta\alpha^{(phys)} = \Delta\beta^{(phys)} = \frac{\Delta\alpha^{(elem)}}{pg} = \frac{\Delta\beta^{(elem)}}{pg}$. The GLL points are located at [add GLL locations....](#). The interpolation is performed in central-angle coordinates using tensor product cubic interpolation ([maybe cite ECMWF techinal report](#)). For elements located on a cubed-sphere edge or corner the coordinate system for neighboring elements may be on a different panel. To take into account this coordinate change the central angle locations of physics grid cell centers located on other panels are transformed to the coordinate system of the panel the element in question is located on (the transformations are given in, e.g., Nair et al. 2005). An illustration is given in Figure A1 for an element located in the lower left corner of a panel. The element in question is $(\xi, \chi) \in (-1, 1)^2$ where, for simplicity, we have transformed the element coordinates into normalized coordinates $(\xi, \chi) = \left(\frac{2(\alpha^{(phys)} - \alpha_1^{(elem)})}{\Delta\alpha^{(elem)}} - 1, \frac{2(\beta^{(phys)} - \beta_1^{(elem)})}{\Delta\beta^{(elem)}} - 1 \right)$

In this coordinate system the center of the physics grid cells are located at

$$(\xi_i^1, \xi_j^2) = \left[-1 + \left(i - \frac{1}{2} \right) \times \Delta\xi, + \left(j - \frac{1}{2} \right) \times \Delta\xi \right], \quad (A2)$$

References

- Arakawa, A., and W. H. Schubert, 1974: Interaction of a cumulus cloud ensemble with the large-scale environment, Part I. *J. Atmos. Sci.*, **31**, 674–701.
- Bacmeister, J. T., and Coauthors, 2018: Projected changes in tropical cyclone activity under future warming scenarios using a high-resolution climate model. *Climatic Change*, **146**, 547–560, doi:10.1007/s10584-016-1750-x, URL <http://dx.doi.org/10.1007/s10584-016-1750-x>.
- Brdar, S., M. Baldauf, A. Dedner, and R. Klfkorn, 2013: Comparison of dynamical cores for nwp models: comparison of cosmo and dune. *Theoretical and Computational Fluid Dynamics*, **27** (3-4), 453–472, doi:10.1007/s00162-012-0264-z.
- Dennis, J. M., and Coauthors, 2012: CAM-SE: A scalable spectral element dynamical core for the Community Atmosphere Model. *Int. J. High. Perform. C.*, **26** (1), 74–89, doi:10.1177/1094342011428142, URL <http://hpc.sagepub.com/content/26/1/74.abstract>, <http://hpc.sagepub.com/content/26/1/74.full.pdf+html>.
- Durrant, D., 2010: *Numerical Methods for Fluid Dynamics: With Applications to Geophysics*, Texts in Applied Mathematics, Vol. 32. 2nd ed., Springer, 516 p.
- Fournier, A., M. A. Taylor, and J. J. Tribbia, 2004: The spectral element atmosphere model (SEAM): High-resolution parallel computation and localized resolution of regional dynamics. *Mon. Wea. Rev.*, **132** (3), 726–748.
- Giraldo, F., and M. Restelli, 2008: A study of spectral element and discontinuous galerkin methods for the Navier-Stokes equations in nonhydrostatic mesoscale atmospheric modeling: Equation sets and test cases. *J. Comput. Phys.*, **227** (8), 3849 – 3877, doi:<http://dx.doi.org/10.1016/j.jcp.2007.12.009>.
- Guba, O., M. Taylor, and A. St-Cyr, 2014a: Optimization-based limiters for the spectral element method. *J. Comput. Phys.*, **267** (0), 176 – 195, doi:<http://dx.doi.org/10.1016/j.jcp.2014.02.029>.
- Guba, O., M. A. Taylor, P. A. Ullrich, J. R. Overfelt, and M. N. Levy, 2014b: The spectral element method (sem) on variable-resolution grids: evaluating grid sensitivity and resolution-aware numerical viscosity. *Geosci. Model Dev.*, **7** (6), 2803–2816, doi:10.5194/gmd-7-2803-2014.
- Held, I. M., and M. J. Suarez, 1994: A proposal for the intercomparison of the dynamical cores of atmospheric general circulation models. *Bull. Am. Meteorol. Soc.*, **73**, 1825–1830.
- Kim, Y.-J., F. X. Giraldo, M. Flatau, C.-S. Liou, and M. S. Peng, 2008: A sensitivity study of the kelvin wave and the Madden-Julian oscillation in aquaplanet simulations by the Naval Research Laboratory Spectral Element Atmospheric Model. *J. Geo. Res.: Atmospheres*, **113** (D20), doi:10.1029/2008JD009887, d20102.
- Lauritzen, P. H., M. A. Taylor, J. Overfelt, P. A. Ullrich, R. D. Nair, S. Goldhaber, and R. Kelly, 2017: CAM-SE-CSLAM: Consistent coupling of a conservative semi-lagrangian finite-volume method with spectral element dynamics. *Mon. Wea. Rev.*, **145** (3), 833–855, doi:10.1175/MWR-D-16-0258.1.
- Lauritzen, P. H., and Coauthors, 2018: Ncar cesm2.0 release of camse: A reformulation of the spectral-element dynamical core in dry-mass vertical coordinates with comprehensive treatment of condensates and energy. *J. Adv. Model. Earth Syst.*, revised.
- Medeiros, B., D. L. Williamson, and J. G. Olson, 2016: Reference aquaplanet climate in the community atmosphere model, version 5. *J. Adv. Model. Earth Syst.*, **8** (1), 406–424, doi:10.1002/2015MS000593.
- Nair, R., H.-W. Choi, and H. Tufo, 2009: Computational aspects of a scalable high-order discontinuous galerkin atmospheric dynamical core. *Computers & Fluids*, **38** (2), 309 – 319, doi:<http://dx.doi.org/10.1016/j.compfluid.2008.04.006>.
- Nair, R. D., M. N. Levy, and P. H. Lauritzen, 2011: Emerging numerical methods for atmospheric modeling, in: P.H. Lauritzen, R.D. Nair, C. Jablonowski, M. Taylor (Eds.), Numerical techniques for global atmospheric models. *Lecture Notes in Computational Science and Engineering*, Springer, **80**.
- Nair, R. D., S. J. Thomas, and R. D. Loft, 2005: A discontinuous galerkin transport scheme on the cubed sphere. *Mon. Wea. Rev.*, **133** (4), 814–828, doi:10.1175/MWR2890.1.
- Neale, R. B., and B. J. Hoskins, 2000: A standard test for agcm's including their physical parametrizations: I: the proposal. *Atmos. Sci. Lett.*, **1** (2), 101–107, doi:10.1006/asle.2000.0022.
- Neale, R. B., and Coauthors, 2012: Description of the NCAR Community Atmosphere Model (CAM 5.0). NCAR Technical Note NCAR/TN-486+STR, National Center of Atmospheric Research.
- Plant, G. C. C., R. S., 2008: A stochastic parameterization for deep convection based on equilibrium statistics. *J. Atmos. Sci.*, **65**, 87–105, doi:10.1175/2007JAS2263.1, URL <http://dx.doi.org/10.1175/2007JAS2263.1>.
- Reed, K. A., J. T. Bacmeister, N. A. Rosenbloom, M. F. Wehner, S. C. Bates, P. H. Lauritzen, J. E. Truesdale, and C. Hannay, 2015: Impact of the dynamical core on the direct simulation of tropical cyclones in a high-resolution global model. *Geophys. Res. Lett.*, **42** (9), 3603–3608, doi:10.1002/2015GL063974.
- Rhoades, A. M., X. Huang, P. A. Ullrich, and C. M. Zarzycki, 2016: Characterizing sierra nevada snowpack using variable-resolution cesm. *Journal of Applied Meteorology and Climatology*, **55** (1), 173–196, doi:10.1175/JAMC-D-15-0156.1, URL <https://doi.org/10.1175/JAMC-D-15-0156.1>.
- Small, R. J., and Coauthors, 2014: A new synoptic scale resolving global climate simulation using the community earth system model. *Journal of Advances in Modeling Earth Systems*, **6** (4), 1065–1094, doi:10.1002/2014MS000363.
- Taylor, M., J. Edwards, and A. St-Cyr, 2008: Petascale atmospheric models for the community climate system model: new developments and evaluation of scalable dynamical cores. *J. Phys.: Conf. Ser.*, **125**, doi:10.1088/1742-6596/125/1/012023.
- Taylor, M. A., and A. Fournier, 2010: A compatible and conservative spectral element method on unstructured grids. *J. Comput. Phys.*, **229** (17), 5879 – 5895, doi:10.1016/j.jcp.2010.04.008.
- Ullrich, P. A., D. Devendran, and H. Johansen, 2016: Arbitrary-order conservative and consistent remapping and a theory of linear maps: Part ii. *Mon. Wea. Rev.*, **144** (4), 1529–1549, doi:10.1175/MWR-D-15-0301.1.
- Ullrich, P. A., and M. A. Taylor, 2015: Arbitrary-order conservative and consistent remapping and a theory of linear maps: Part I. *Mon. Wea. Rev.*, **143**, 2419–2440, doi:10.1175/MWR-D-14-00343.1.

Zarzycki, C. M., C. Jablonowski, and M. A. Taylor, 2014a: Using variable-resolution meshes to model tropical cyclones in the community atmosphere model. *Mon. Wea. Rev.*, **142** (3), 1221–1239, doi: 10.1175/MWR-D-13-00179.1.

Zarzycki, C. M., M. N. Levy, C. Jablonowski, J. R. Overfelt, M. A. Taylor, and P. A. Ullrich, 2014b: Aquaplanet experiments using cam's variable-resolution dynamical core. *J. Climate*, **27** (14), 5481–5503, doi:10.1175/JCLI-D-14-00004.1.